NRC Research Press

ARTICLE

Strain-softening model evaluating geobelt–clay interaction validated by laboratory tests of sensor-enabled geobelts

Xin-zhuang Cui, Yi-lin Wang, Kai-Wen Liu, Jun Li, Lei Zhang, and Jun-wei Su

Abstract: The interaction between geosynthetics and soil is vital for the stability and the bearing capacity of geosynthetic-reinforced soil structures. This contact behavior between geosynthetics and granular soils has been extensively studied in the literature while there is scarcity of it related to geosynthetics and cohesive soils particularly with softening responses. This paper presents a strain-softening model of geobelt–clay interaction based on direct shear test results under two compaction degrees. A theoretical model for evaluating the pullout behavior of a geobelt is proposed by employing the strain-softening model verified by direct shear tests and a hyperbolic model capturing the stress–strain curves of a geobelt calibrated by uniaxial tensile tests. The proposed model is numerically solved and validated by pullout tests. A kind of sensor-enabled geobelt (SEGB) was adopted in all the aforementioned tests. Both test and numerical results show an overall softening trend in terms of front pull-out force versus displacement. Generally, the model proposed can give reasonably good agreement between calculations and test data during the whole pull-out range. Also, the strain distributions measured by SEGBs demonstrate the working process during the pullout tests, which makes SEGBs a potentially new choice for the strain measurements of in-soil geobelts.

Key words: strain-softening model, geobelt–clay interaction, pullout test, sensor-enabled geobelts, numerical solution.

Résumé : L'interaction entre les géosynthétiques et le sol est vitale pour la stabilité et la capacité portante des structures de sol renforcé de géosynthétiques. Ce comportement de contact entre les géosynthétiques et les sols granulaires a fait l'objet d'études approfondies dans la littérature, alors qu'il y a absence d'études liées aux géosynthétiques et sols cohésifs, en particulier aux réponses d'adoucissement. Cet article présente un modèle d'adoucissement de la déformation de l'interaction « geobelt »–argile (où geobelt est une bandelette géotextile) basé sur les résultats d'essais de cisaillement direct sous deux degrés de compactage. Un modèle théorique d'évaluation du comportement à l'arrachement de la bandelette géotextile est proposé en utilisant le modèle d'adoucissement de la contrainte vérifié par des essais de cisaillement direct et un modèle hyperbolique capturant les courbes contrainte–déformation de la bandelette géotextile calibrées par des essais de traction uniaxiale. Le modèle proposé est résolu numériquement et validé par des essais d'arrachement. Une sorte de bandelette géotextile à capteurs (« SEGB ») a été adoptée dans tous les essais susmentionnés. Les résultats des essais et les résultats numériques montrent une tendance générale à la baisse de la force d'arrachement avant en fonction du déplacement. En général, le modèle proposé peut donner une assez bonne concordance entre les calculs et les données d'essai pour l'ensemble de la plage d'arrachement. De plus, les distributions de déformation mesurées par SEGB démontrent le processus de travail pendant les essais d'arrachement, ce qui fait de SEGB un choix potentiellement nouveau pour les mesures de déformation des bandelettes géotextiles dans le sol. [Traduit par la Rédaction]

Mots-clés : modèle d'adoucissement de la déformation, interaction « geobelt » (bandelette géotextile)–argile, essai d'arrachement, bandelettes géotextiles équipées de capteurs, solution numérique.

Introduction

In recent years, geosynthetics have been extensively employed in geotechnical engineering practice to reinforce soils and improve the overall performance of foundations (Chen and Abu-Farsakh 2016; Shahin et al. 2017; Yu and Bathurst 2017*a*), embankments (Rowe and Liu 2015; Chawla and Shahu 2016; Yu et al. 2016*a*; Yu and Bathurst 2017*b*; H.B. Liu et al. 2017*a*; K.W. Liu et al. 2017, 2018; Shen et al. 2018), and walls (Xie and Leshchinsky 2015; Liu 2016; Yu et al. 2016*b*; Yu and Bathurst 2017*c*; H.B. Liu et al. 2017*b*; Zhang et al. 2018). The stability and the bearing capacity of the geosynthetic-reinforced soil structures (GRSS) are mainly enhanced and improved by the competent interactions between the geosynthetics and surrounding soils. Thus, the study of the geosynthetic–soil interaction is very important from stability considerations and has been a consistent concern of the geotechnical engineering community.

Direct shear tests and pullout tests are both effective to investigate the diverse kinds of interaction between geosynthetics and soil. Many researchers have performed experimental investigations on the interactions between different soils and various geosynthetics. Racana et al. (2003) conducted pullout tests of geobelts (or geotextile strips) in sand to verify the independently developed numerical model. Abdelouhab et al. (2010) established physical and analytical modelling for the pullout behavior of two types of geobelts. Choudhary and Krishna (2016) carried out direct shear tests and pullout tests to investigate the interactions of three different cohesionless soils and three different geosynthetics — nonwoven geotextile, woven geotextile, and geogrid. Bathurst and Ezzein (2017) carried out pullout tests on geogrids with a

Received 14 August 2018. Accepted 13 April 2019.

X.-z. Cui, Y.-l. Wang, J. Li, L. Zhang, and J.-w. Su. School of Civil Engineering, Shandong University, Jinan 250061, China.
K.-W. Liu.* Key Laboratory of High-Speed Railway Engineering, Ministry of Education, Southwest Jiaotong University, Chengdu 610031, China.
Corresponding author: Kai-Wen Liu (email: kaiwen.liu@queensu.ca).

*K.-W. Liu currently serves as an Editorial Board Member; peer review and editorial decisions regarding this manuscript were handled by E.M. Palmeira.

transparent granular soil to investigate the load transfer between the transverse members and the granular soils. Mousavi (2017) conducted direct shear tests and pullout tests to evaluate the influences of soil contamination on the shear strength behavior at the interfaces with various geosynthetics including geotextile, geomembrane, and geogrid. Wang et al. (2017) developed a large direct shear test apparatus equipped with visualization and data acquisition system. The study investigated the interaction of geogrid and coarse-grained soil with the new apparatus and the influence of transverse ribs of geogrids on the interface was evaluated.

In the literature, extensive research has been focused on geosynthetic-reinforced granular soils while the number of studies on the geosynthetic-reinforced cohesive soils is relatively limited. In practice, granular soils are not always available on site where the use of cohesive soils can give significant savings (e.g., Zornberg and Mitchell 1994; Mitchell and Zornberg 1995). There is a gradual increase in research interest in the behavior of geosynthetic-reinforced cohesive slopes–retaining walls–subgrades of railways in both laboratory and filed scales (e.g., Portelinha et al. 2013; Chawla and Shahu 2016; Abd and Utili 2017). Many studies have demonstrated that the interfacial behaviors vary with the types of both geosynthetics and surrounding soils through experiments (Infante et al. 2016). Rousé et al. (2014) reported that two different interfacial responses (hardening and softening) were observed in the interaction of two different textured planar inclusions embedded in sand. Mosallanezhad et al. (2016) presented the hardening behavior at the geogrid–sand interface during pullout tests. Wang et al. (2016) found that soils at interfaces all showed hardening for geobelts (geogrids without transverse ribs) although softening was also observed for other geogrids under the same stress condition. Many researchers have reported the interfacial shear stresses showing hardening response with shear displacements (e.g., Gurung and Iwao 1999; Punetha et al. 2017; Sadat Taghavi and Mosallanezhad 2017). The shear stress softening was mostly observed in the interaction between geosynthetics and clayey soils (e.g., Chai and Saito 2016). Only a few researchers have attempted to establish analytical models considering softening interfacial responses. For instance, Tano et al. (2017) developed a numerical modelling technique capturing strain-softening at interfaces and established a two-dimensional finite-difference model on a reinforced geosynthetic system over a cavity. Therefore, further research on the interaction between geosynthetics and clay, particularly with softening responses, is in high demanded.

Some researchers have established different strain-softening models. Seo et al. (2004) presented constitutive models for two strain-softening interfaces with a smooth peak and a sharp peak. In these two constitutive models, the strain-softening responses at the interfaces were separated as pre-peak stage and post-peak stage. The constitutive models were both piecewise functions. The pre-peak stage in the strain-softening response was simulated with a hyperbolic model or a linear model, while the post-peak stage was approximated as nonlinear hyperbolic relation described by Esterhuizen et al. (2001). The same method was also employed by Anubhav and Basudhar (2010). The aforementioned models combining piecewise functions involve many parameters. Therefore, developing an efficient constitutive model with relatively less parameters is another objective of this paper.

In this paper, a theoretical model for evaluating the pullout behavior of the geobelt is established by employing two models. One is the aforementioned strain-softening model, and the other one is a hyperbolic model capturing the stress–strain relation of geobelts. The load transfer equation is deduced and numerically solved. The specimens used in direct shear tests and pullout tests are sensor-enabled geobelts (SEGBs). The tensoresistivity performance of SEGBs enables the strains of geobelts to be measured based on piezoresistive effect, which could be utilized as a potentially new method for the strain measurement of in-soil geobelts. The numerical results from theoretical models are compared with pullout test results, including the measurements of SEGBs. Based on the theoretical model validated, the influence of compaction degree on pullout behavior is discussed and the measurement function of SEGBs is evaluated.

Fig. 1. Particle-size distribution of clay tested.

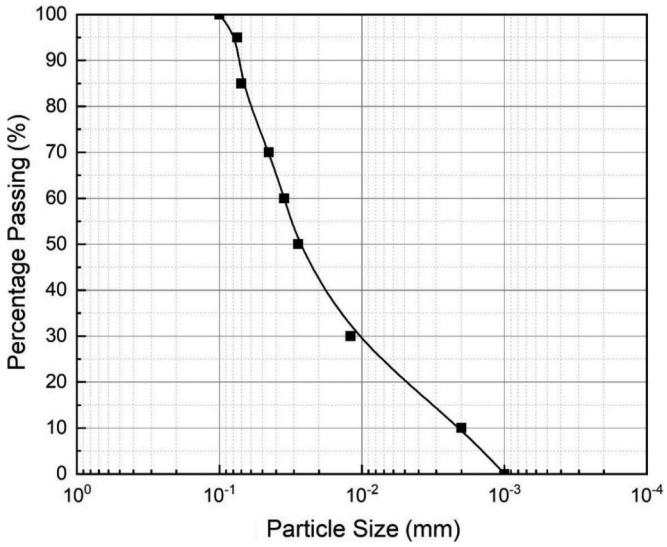

Laboratory tests of geobelt–soil interaction

Backfill material

The soil used in tests is classified as low liquid limit clay (CL) according to the Unified Soil Classification System (ASTM 2011) with the particle-size distribution shown in Fig. 1. The uniformity coefficient (C_u) and the coefficient of curvature (C_c) were 17.50 and 2.06, respectively. The liquid limit w_L was 26.0% and the plasticity index I_P was 8.7. The maximum dry density and the optimum water content were 1.85 g/cm^3 and 13.5%, respectively. Direct shear test carried out on an intact sample of clay (natural water content of 8.6%) showed values of apparent cohesion and frictional angle equal to 136.9 kPa and 33.7°, respectively. In direct shear tests and pullout tests, the clay was compacted by layers with two compaction degrees of 90% and 96%, respectively. Each layer of compaction was 50 mm thick.

Geobelt

The geobelt used in this paper was a SEGB derived from an original material nominated sensor-enabled geosynthetic (SEG), developed by Hatami et al. (2009). The conception of preliminary product and basic features at the laboratory presented by Hatami et al. (2009) were followed to improve the manufacturing process of SEGB and to evaluate pilot tests — reported by Cui et al. (2018*a*) and Li et al. (2018) — on mechanical and electrical properties. As a polymer composite made from high-density polyethylene (HDPE), the industry-fabricated SEGB samples are molded as thin plates with the thickness of 1.8 mm. The thin plate-shaped samples could be cut into individual specimens (geobelts or geogrids) with required dimensions. The widths of specimens in tensile load tests and pullout tests are 1.5 and 40 mm, respectively.

By mixing the masterbatch of carbon black with HDPE, the SEGB exhibited conductivity and tensoresistivity, which enabled the strain of SEGB to be acquired by measuring the changes of electrical resistance. Tensoresistivity test results (Cui et al. 2018*a*, 2018*b*, 2019) suggested the strain determination method as follows:

Fig. 2. Diagram of SEGB specimen sealed with HPP (reproduced from Cui et al. 2018*a*). [Color online.]

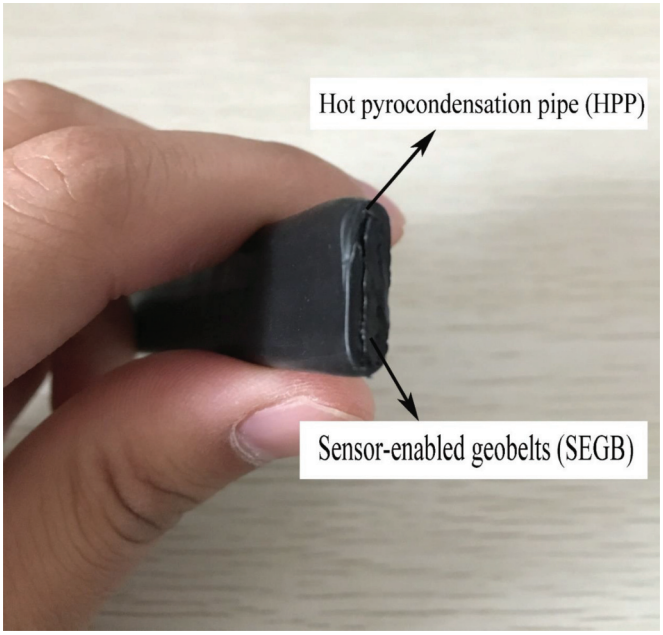

$$\frac{R_s}{R_0} = \alpha\varepsilon^2 + \beta\varepsilon + 1 \quad (1)$$

where R_s is measured value of electrical resistance after deformation; R_0 is initial value of electrical resistance; and the coefficients α and β are constants only related to the materials. According to Cui et al. (2018*b*), values of $\alpha = 0.01599$ and $\beta = 0.1853$ are updated in this study, and the values of α and β are related to a specific SEGB (industry-fabricated and with carbon black–HDPE equal to 45%).

Due to the electrical resistance measurement involved, the SEGB is required to be insulated from water or corrosion in the surroundings. Cui et al. (2018*a*) chose hot pyrocondensation pipes (HPP) as the insulate coating of SEGB (as shown in Fig. 2). Hot melt adhesives were applied on the inner surface of the HPP to enhance the connection between the SEGB and HPP. Due to the hot melt adhesives and the rhombic texture of the SEGB, the cohesion between SEGB and HPP is much greater than the interfacial shear stress between HPP and soil. Considering no slippage between SEGB and HPP before the rupture of SEGB, the measured strains from SEGB could reasonably represent the strain of HPP. The employment of HPP increased the cross-sectional dimensions by 1 mm both in width and thickness. In this paper, all the SEGBs refer to the SEGB specimens covered with the HPP. The specifications of SEGB used in this paper are tabulated in Table 1.

Geobelt–soil interface shear strength tests

The upper shear box and the lower shear box had the same size with the dimension of 500 mm × 500 mm × 200 mm, but only the upper shear box was fixed in the horizontal direction, as shown in Fig. 3. The lower shear box could horizontally move with low friction on stainless wheels, which were lining up along two tracks. The maximum displacement of the lower shear box was 200 mm, which was controlled by stoppers on the tracks. An electrical motor horizontally pushed the lower shear box with a constant displacement rate of 1.0 mm/min. The gap between the lower and upper shear boxes was adjusted to 4.0 mm, slightly larger than the thickness of the testing specimen. The vertical load was applied by a hydraulic jack. The displacements of the lower shear box were measured by linear variable differential transducer (LVDT). The horizontal push force and vertical force were recorded by force sensors.

Table 1. Dimensions of SEGB used in tests.

	Dimensions (including HPP)		
Test	Effective length (mm)	Width (mm)	Thickness (mm)
Uniaxial tensile test	100	16	2.7
Pullout test	600	41	2.7

The testing procedures followed the ASTM (2017) D5321 standard. In direct shear tests, the SEGB + HPP was tested as a plate with large enough size that could exceed the shearing area. The exceeding part of SEGB + HPP was tightly wrapped around a wood block. The wood block was anchored to the front of the lower shear box before filling the clay in the upper shear box as was done by Xiao et al. (2015). The SEGB + HPP did not slide during the direct shear tests. The normal pressures in shear box tests were 30, 50, and 100 kPa. The test cases were tabulated in Table 2.

Geobelt tensile load tests

To obtain the stress–strain curves of SEGBs, uniaxial tensile tests were performed on a universal testing machine. The testing procedures followed ASTM (2007) standard D6637-01. The SEGB specimens were 100 mm long, 16 mm wide, and 2.7 mm thick.

Figure 4 shows the full tensile stress–strain curves of SEGB specimens loaded with strain rate of 1%/min, 5%/min, and 10%/min. The tensile stress of the specimen increased rapidly in the early stage until a peak value and then the stress maintained at the peak value until rupture.

Geobelt pullout tests

A schematic diagram for the large pullout apparatus developed by authors is shown as Fig. 5. The apparatus consisted of four parts: test chamber, horizontal pulling system, vertical loading system, and force sensor system. The SEGB specimen was embedded in compacted clay in the 800 mm long × 400 mm wide × 550 mm high test chamber. The front end of the SEGB specimen extended through a gap in the front wall of the test chamber and was fixed on a clamp. To prevent the soil particles from running through the gap, a restraint was closely placed to the inner side of the front wall. The inner sides of the sidewalls were greased and then covered with thin sheets of polyethylene films to reduce the friction due to the soil particles. The system for applying the pulling load to the SEGB involved a screw powered by an electric servomotor. The servomotor ensured that the clamp moved at a constant displacement rate set as 1.0 mm/min. The SEGB was clamped between two rubber sheets that were held between two steel plates by five high-strength bolts. It was assumed that connection system worked well because no rupture of SEGB was observed on the plates. The vertical loading system comprised a hydraulic jack attached to a reaction frame on one end and two I-beams on the other end. The two I-beams with a length of 600 mm were deployed abreast on a bearing plate to apply a normal pressure as uniform as possible. The bearing plate was a 10 mm thick steel plate to cover the test chamber. The force sensor system comprised two force sensors. One of the sensors monitored the tension induced by the screw in the horizontal pulling system; the other one was attached to the vertical loading system to monitor the pressure from hydraulic jacks.

The pullout test procedures followed ASTM (2013) standard D6706-01. The SEGB specimens were made with dimensions: width of 41 mm and length of 600 mm. By attaching wires, the electrical resistance between two adjacent attached nodes could be measured. The wires were mixed with hot melt adhesives and wrapped by HPP as shown in Fig. 6. There were 11 measuring points uniformly distributed along the specimen with a spacing of

Fig. 3. Large-scale direct shear test device. [Color online.]

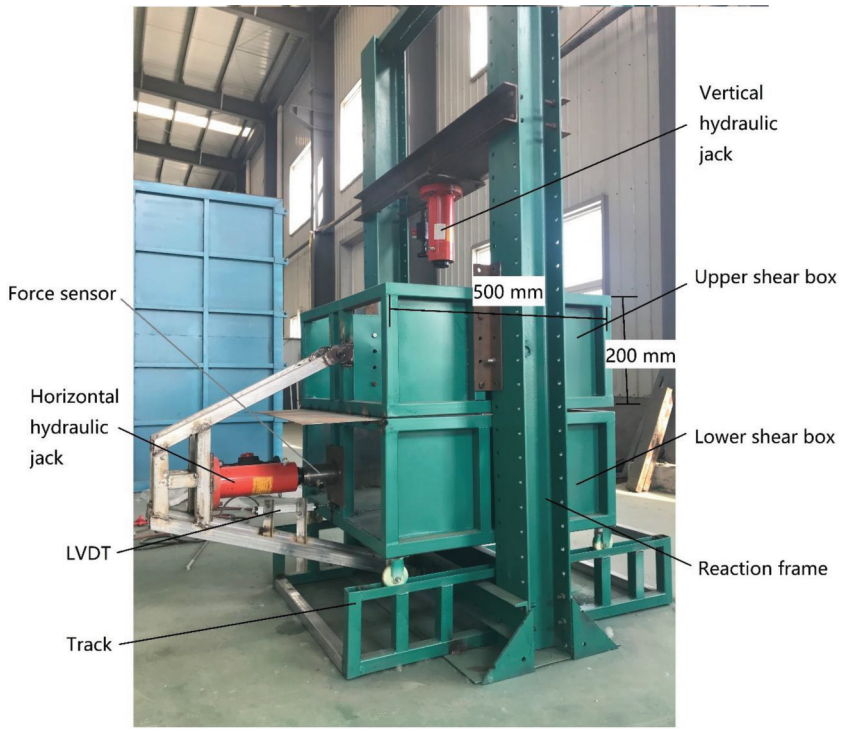

Table 2. Cases of direct shear test.

Case	Normal pressure, σ_v (kPa)	Degree of compaction (%)
1	30	90
2	50	90
3	100	90
4	30	96
5	50	96
6	100	96

60 mm. Note that the electrical resistance values must be measured between adjacent measuring points. The normal pressures in pullout tests were 30, 50, and 100 kPa. Pullout tests and direct shear tests were carried out with clay at the same compaction degree. Test cases are summarized in Table 3.

Simplified strain-softening model of geobelt–clay interaction

Basic concept of model

Direct shear test results indicated that the shear response of geobelt–clay interface followed a strain-softening model as shown in Fig. 7. In the strain-softening model, the shear stress acting along the interface increases nonlinearly with the increasing of displacement until the peak in pre-peak stage and decreases until approaching a residual value in post-peak stage. When the displacement reaches the value u_m, the interfacial shear stress achieves the maximum value, τ_m. The shear stress then decreases with increasing displacement.

The strain-softening behavior between the interfacial shear stress and relative shear displacement could be described by the following equation (Zhang and Zhang 2012):

$$\tau = \frac{u(p + qu)}{(p + ru)^2} \quad (2)$$

Fig. 4. Tensile stress–strain curves for SEGB specimens. [Color online.]

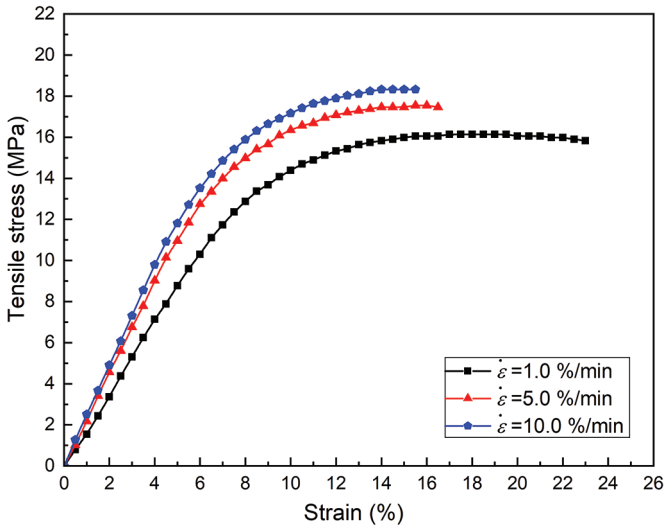

where τ is the interfacial shear stress; u is the interface relative shear displacement; p, q, and r are the parameters related to soil and geobelt.

Determination of values of parameters in strain-softening model

When the shear displacement reaches the value of u_m, the interfacial shear stress achieves the maximum value, τ_m.

The derivative of eq. 2 is written as

$$\frac{d\tau}{du} = \frac{[(p + 2qu)(p + ru) - 2ru(p + qu)]}{(p + ru)^3} \quad (3)$$

The value of u_m can be estimated by following the assumption that the derivative of eq. 2 equals to zero:

Fig. 5. Schematic diagram of pullout test apparatus: 1, reaction frame; 2, pressure sensor; 3, hydraulic jack; 4, I-beam; 5, bearing plate; 6, vertical loading system; 7, test chamber; 8, restraint; 9, soil; 10, conductive adhesive tapes; 11, SEGB; 12, clamp; 13, high-strength bolts; 14, rubber sheet; 15, tensor sensor; 16, driving screw; 17, electric servomotor; 18, horizontal pulling system.

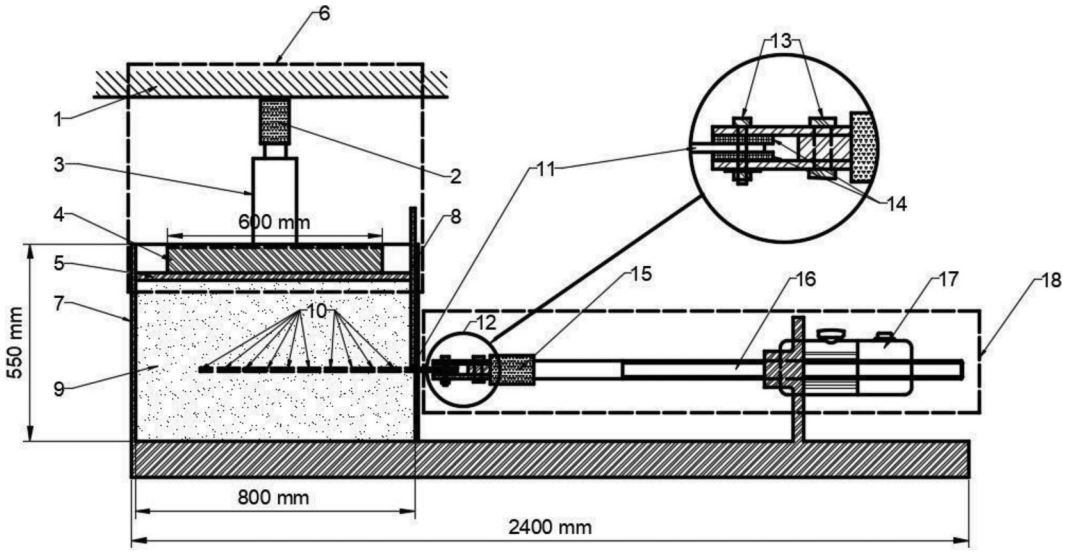

Fig. 6. Cross-section illustration of SEGB sealed with HPP (reproduced from Cui et al. 2018*a*).

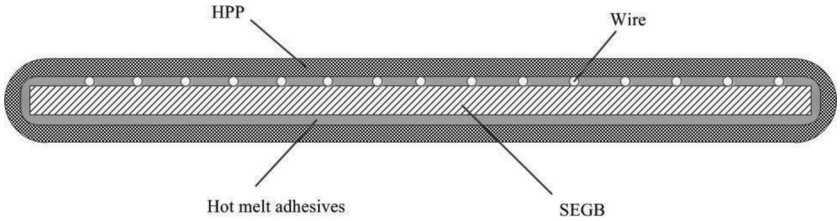

Table 3. Cases of pullout test.

Case	Normal pressure, σ_v (kPa)	Degree of compaction (%)
1	30	90
2	50	90
3	100	90
4	30	96
5	50	96
6	100	96

$$\frac{d\tau}{du} = 0 \Rightarrow u_m = \frac{p}{r - 2q} \quad (4)$$

The slope of the tangent line at the original point is the initial shear modulus of geobelt–clay interface (E_s), which could be obtained by the following equation:

$$E_s = \left.\frac{d\tau}{du}\right|_{u=0} = \frac{1}{p} \quad (5)$$

By substituting eq. 4 into eq. 2, the value of τ_m could be obtained in the following form:

$$\tau_m = \tau(u_m) = \frac{1}{4(r - q)} \quad (6)$$

When the shear displacement reaches a very large value (u_∞), the interfacial shear stress remains at a residue value (τ_r). The value of τ_r can be calculated using the following equation:

Fig. 7. Assumed relationship between shear stress and shear displacement.

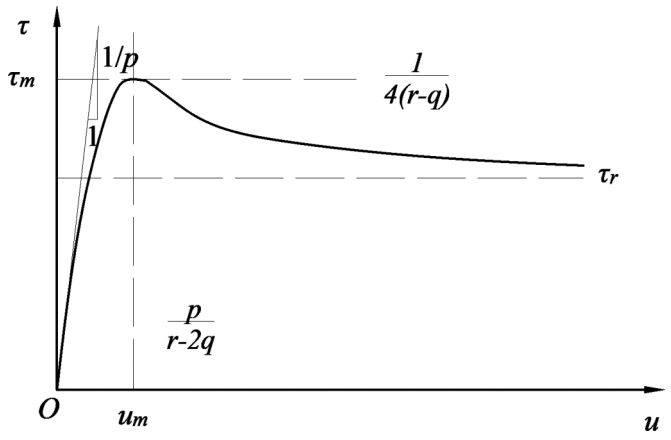

$$\tau_r = \lim_{u\to\infty} \frac{u(p + qu)}{(p + ru)^2} = \frac{q}{r^2} = \beta_r \tau_m \quad (7)$$

where β_r is defined as the ratio of the residual shear stress to the maximum shear stress at the interfaces. The value of β_r could be obtained by back-analysis of direct shear test results.

From eqs. 6 and 7, the value of the parameter r could be expressed as

$$r = \frac{1 - \sqrt{1 - \beta_r}}{2\beta_r} \frac{1}{\tau_m} \quad (8)$$

Fig. 8. Shear stress–shear displacement curves: (*a*) compaction degree of 90%; (*b*) compaction degree of 96%. [Color online.]

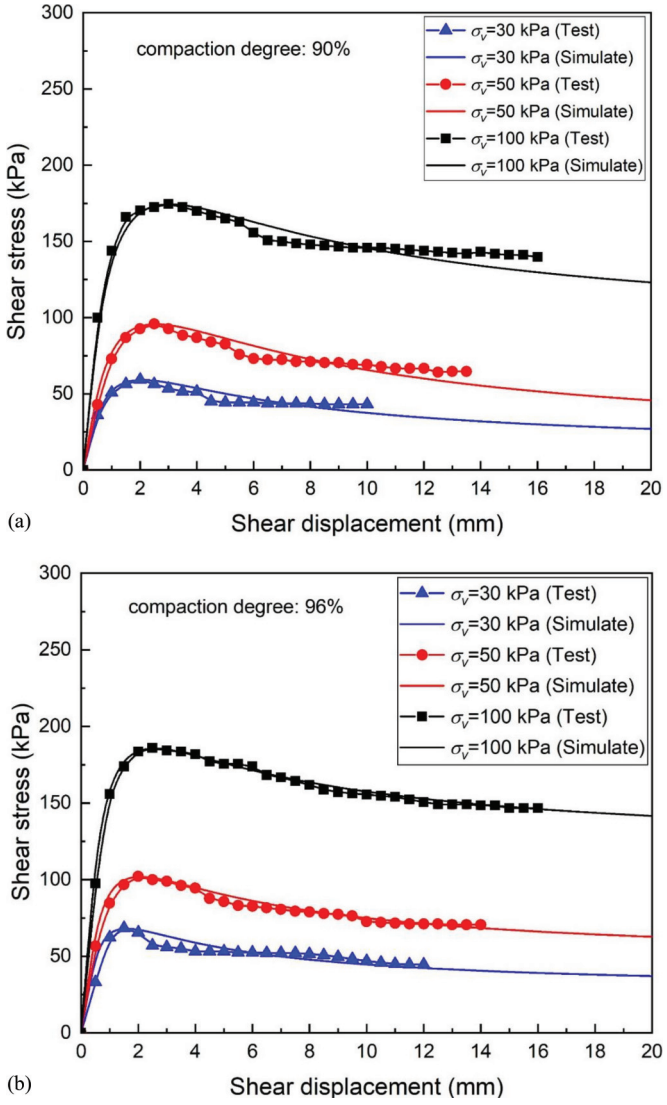

Fig. 9. Shear stress–normal pressure curves: (*a*) compaction degree of 90%; (*b*) compaction degree of 96%. [Color online.]

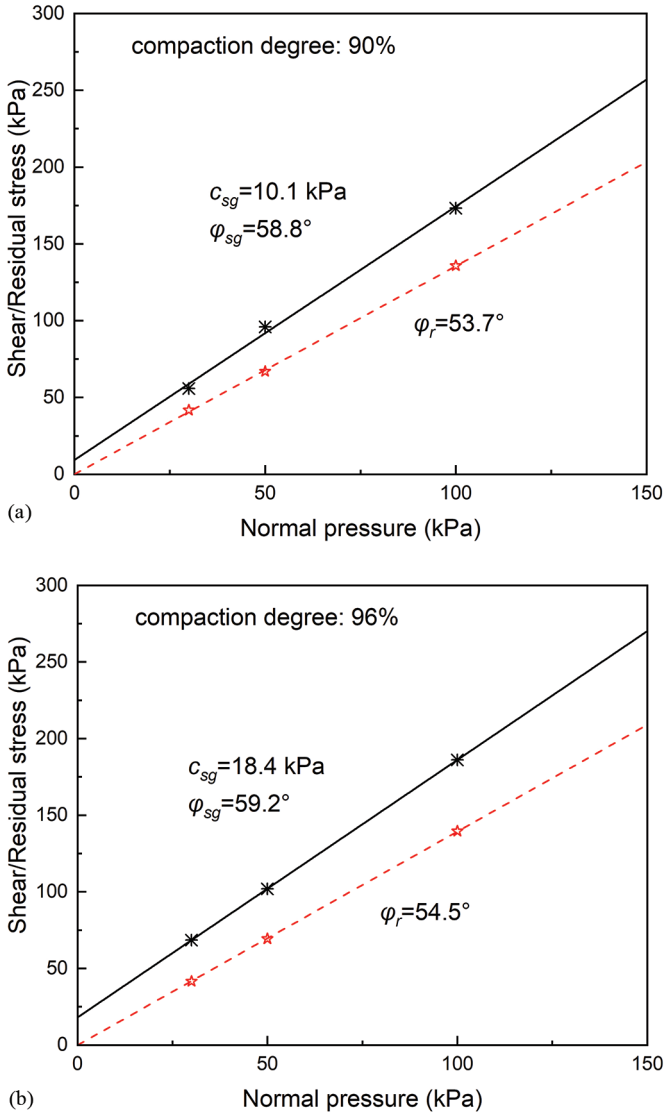

By substituting eq. 8 into eq. 6, the value of the parameter q could be expressed as

$$q = \frac{2 - \beta_r - 2\sqrt{1-\beta_r}}{4\beta_r}\frac{1}{\tau_m} \quad (9)$$

Combining eqs. 4, 8, and 9, the value of parameter p could be obtained as

$$p = (r - 2q)u_m = \frac{\beta_r - 1 + \sqrt{1-\beta_r}}{2\beta_r}u_m \quad (10)$$

Note that only the value of r resulting in the positive initial shear modulus of the geobelt–clay interface (E_s) is provided. The maximum value of shear stress or the shear strength (τ_m) could be obtained by Mohr–Coulomb's friction law

$$\tau_m = c_{sg} + \sigma_v \tan\varphi_{sg} \quad (11)$$

where c_{sg} is the peak apparent cohesion of interfacial friction; σ_v is the vertical pressure; and φ_{sg} is the peak angle of interfacial friction.

Shear response of geobelt–clay interfaces

Based on the shear stress–shear displacement curves obtained from direct shear tests, the strain-softening models could be established for compaction degrees of 90% and 96%, respectively, as shown in Figs. 8*a* and 9*a*. The parameters of the strain-softening model were obtained and tabulated in Table 4.

Figures 8*b* and 9*b* show the variation of the shear strength and the residual stress with normal pressures, respectively. It is observed that for both the compaction degrees, φ_{sg} was larger than the residual angle of interfacial friction (φ_r). The comparison between Figs. 8 and 9 indicates that a higher compaction degree of soil would result in higher interfacial shear stress, including the peak shear stress and the residual shear stress under the same shear displacement. Additionally, c_{sg} increased with the increasing compaction degree. However, φ_{sg} and φ_r had limited increment.

Table 4. Parameters of softening models for geobelt–clay interaction.

Compaction degree (%)	Apparent cohesion, c_{sg} (kPa)	Angle of interfacial friction, φ_{sg} (°)	β_r		
			σ_v = 30 kPa	σ_v = 50 kPa	σ_v = 100 kPa
90	10.1	58.8	0.20	0.15	0.50
96	18.4	59.2	0.40	0.45	0.64

Fig. 10. Back-calculation of a and b for hyperbolic model. [Color online.]

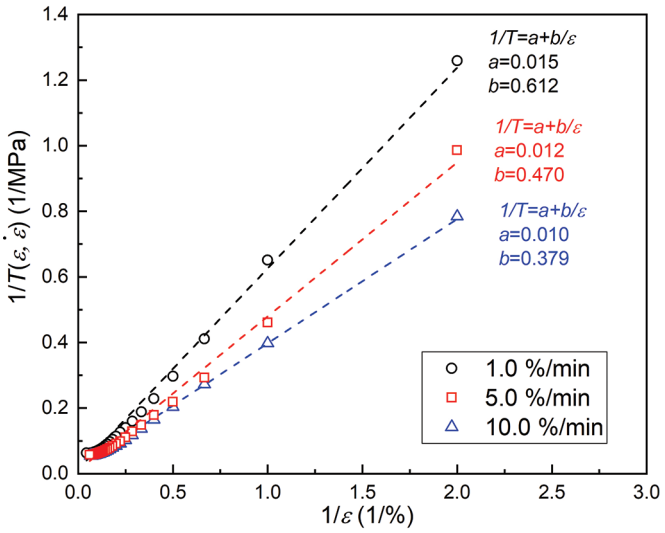

Fig. 11. Hyperbolic model parameters a and b versus strain rate. [Color online.]

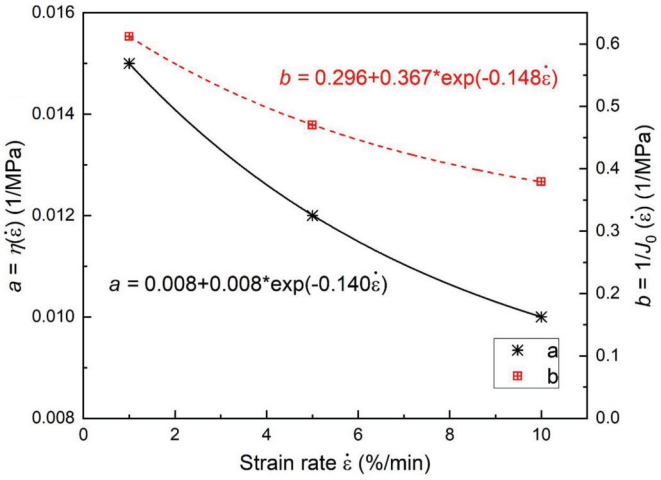

Pullout behavior analysis of geobelt employing strain-softening model

The pullout test is one of the most effective tests to analyze the interaction between geosynthetics and surrounding soil. The pullout behavior of geobelts is closely related to the tensile property of the geobelts and the geobelt–clay interaction. Therefore, the pullout behavior analysis of the geobelts requires the modeling of geobelt–clay interaction, as well as the modeling of tensile property of geobelts.

Hyperbolic model of uniaxial tensile stress–strain curves of SEGB

In this paper, the stress–strain curve of an SEGB specimen is described using a hyperbolic relationship, which is given by the following equation proposed by Ezzein et al. (2015):

$$T(\varepsilon, \dot{\varepsilon}) = \frac{F(\varepsilon, \dot{\varepsilon})}{A} = \frac{\varepsilon}{\frac{1}{J_0(\dot{\varepsilon})} + \eta(\dot{\varepsilon})\varepsilon} \quad (12)$$

where T is the tensile stress of the specimen; ε is the strain of the specimen; $\dot{\varepsilon}$ is the strain rate or the loading speed; F is the tensile force; A is the cross-sectional area of geobelt; J_0 is the strain-rate-dependent initial axial stiffness of geobelt; and η is an empirical strain-rate-dependent scaling factor.

As a hyperbolic function, eq. 12 could be transformed to the following linear form:

$$y = a + bx \quad (13)$$

where $y = 1/T(\varepsilon, \dot{\varepsilon})$, $a = \eta(\dot{\varepsilon})$, $b = 1/J_0(\dot{\varepsilon})$, and $x = 1/\varepsilon$.

This transformation is convenient to find expressions for $J_0(\dot{\varepsilon})$ and $\eta(\dot{\varepsilon})$ by back-analysis to measured stress–strain curves. Figure 10 shows the back-calculated values of a and b by converting the coordinate axes. By linear fitting of the transformed test results, the parameters a and b under the loading speed of 1%/min, 5%/min, and 10%/min could be obtained. Equation 13 gives $J_0(1)$ = 1.63 MPa and $\eta(1)$ = 0.015 MPa^{-1}; $J_0(5)$ = 2.12 MPa and $\eta(5)$ = 0.012 MPa^{-1}; $J_0(10)$ = 2.64 MPa and $\eta(10)$ = 0.01 MPa^{-1}. Ezzein et al. (2015) investigated plenty of test results and suggested the parameters a and b had exponential relations with strain rate, as the following equations:

$$a = \eta(\dot{\varepsilon}) = a_1 + a_2 \exp(-a_3\dot{\varepsilon}) \quad (14)$$

$$b = \frac{1}{J_0(\dot{\varepsilon})} = b_1 + b_2 \exp(-b_3\dot{\varepsilon}) \quad (15)$$

Figure 11 shows the hyperbolic parameters a and b determined by exponential functions of strain rate. By exponentially fitting the measured results at the strain rate of 1.0%/min, 5.0%/min, and 10.0%/min, the parameters in eq. 14 and eq. 15 could be obtained: a_1 = 0.008, a_2 = 0.008, a_3 = 0.14; b_1 = 0.296, b_2 = 0.367, b_3 = 0.148.

Load transfer equation in pullout behavior analysis of geobelt

In this paper, a theoretical model for evaluating the pullout behavior of the geobelt was established by employing two models: (*i*) the strain-softening model established on direct shear tests and (*ii*) the hyperbolic model capturing the stress–strain relation of geobelt. The load transfer equation was deduced and numerically solved.

Figure 12 shows a small differential geobelt element of length dx. Mechanical equilibrium of the element gives

$$dF(x) = -2w\tau(x)[1 + \varepsilon(x)]\,dx \quad (16)$$

where F is the tensile force of the element and w is the width of the geobelt.

Fig. 12. Free-body diagram of SEGB specimen element in pullout tests.

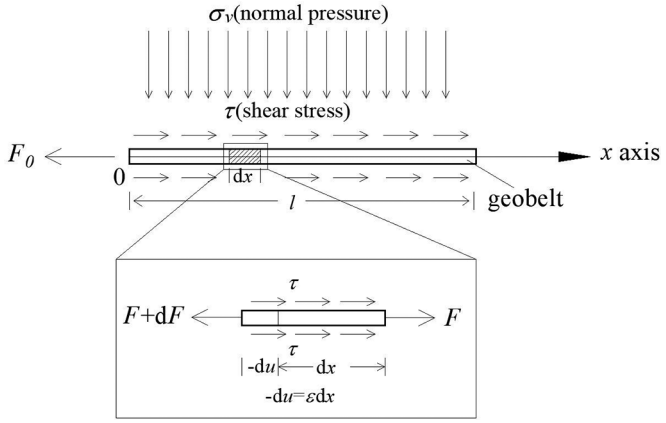

Additionally, the strain of the geobelt can be expressed as

$$\varepsilon(x) = -\frac{du(x)}{dx} \tag{17}$$

The interfacial shear stress τ, the tensile force F, the displacement u, and the strain ε of the geobelt are functions of x. Combined with eqs. 2, 12, 16, and 17, load transfer equations can be obtained:

$$\frac{d^2u(x)}{dx^2} - \frac{2bw}{A}\frac{u(x)[p + qu(x)]}{[p + ru(x)]^2}\left[1 - \frac{du(x)}{dx}\right]\left[1 - \frac{a}{b}\frac{du(x)}{dx}\right]^2 = 0 \tag{18}$$

The boundary conditions of load transfer equations are

$$\begin{aligned} &u(x) = u(0) \quad \text{at } x = 0 \\ &F(x) = 0 \quad \text{or} \quad \frac{du(x)}{dx} = 0 \quad \text{at } x = l \end{aligned} \tag{19}$$

where $u(0)$ is the front displacement from pullout test results; and l is the length of specimen.

Equation 18 can be nondimensionalized and simplified to

$$\frac{d^2U(X)}{dX^2} - \frac{2wbl^2}{A}\frac{U(X)[p + qu_mU(X)]}{[p + ru_mU(X)]^2}\left[1 - \frac{u_m}{l}\frac{dU(X)}{dX}\right] \times \left[1 - \frac{au_m}{bl}\frac{dU(X)}{dX}\right]^2 = 0 \tag{20}$$

where $U = \frac{u(x)}{u_m}$ and $X = \frac{x}{l}$.

The boundary conditions in nondimensionalized form become

$$\begin{aligned} &U(X) = U(0) \quad \text{at } X = 0 \\ &F(X) = 0 \quad \text{or} \quad \frac{dU(X)}{dX} = 0 \quad \text{at } X = 1 \end{aligned} \tag{21}$$

With the boundary conditions eq. 21, the load transfer equation eq. 20 becomes a second order differential equation of boundary value problem. Finite difference method could be used for numerical solutions through the following steps:

1. Discretizing the geobelt into n elements with the proportion of each element, $h = 1/n$, the displacement at node i ($1 \le i \le n$) could be expressed as follows:

$$\frac{U_{i+1} - 2U_i + U_{i-1}}{h^2} - \frac{2wbl^2}{A}\frac{U_i(p + qu_mU_i)}{(p + ru_mU_i)^2} \times \left(1 - \frac{u_m}{l}\frac{U_{i+1} - U_{i-1}}{2h}\right)\left(1 - \frac{au_m}{bl}\frac{U_{i+1} - U_{i-1}}{2h}\right)^2 = 0 \tag{22}$$

2. To solve the displacement at node $i = n$, a fictitious node $i = n + 1$ next to the end of the geobelt (at the node $i = n$) was assumed. The displacements at these nodes can easily be derived with the boundary condition as follows:

$$\begin{aligned} &U_0 = U(0) \\ &(U_{n+1} - U_{n-1})/2h = 0 \end{aligned} \tag{23}$$

3. From the known displacements along the geobelt length, the strain (ε_i) at node i could be calculated as follows:

$$\varepsilon_i = \frac{u_m}{l}\frac{U_{i-1} - U_{i+1}}{2h} \tag{24}$$

4. The interfacial shear stress (τ_i) and the tensile force (F_i) at node i could be calculated by eqs. 2 and 12.

Results and comparison

Validation of numerical results

Figures 13*a* and 13*b* present the comparisons of tested front pullout force–displacement curves and numerical ones with compaction degrees of 90% and 96%, respectively, which both show an overall softening trend. In the pre-peak stage, numerical results showed excellent agreement with test results. In the post-peak stage, the observed trend of softening was well captured by calculations while the magnitude of front force was slightly overestimated. Further, both tested and numerical results indicate that with increasing of the normal pressure and compaction degree, the front displacement required to mobilize the peak value of pullout force decreased. The slight overestimation during the post-peak stage could result from full stress–strain curves predicted by the hyperbolic model. As Fig. 4 shows, although most of the test results are captured, the fitted hyperbolic model overestimates the tensile stress after the yielding of the material. It would result in higher tensile force in calculations, especially for the post-peak stage. On the contrary, the rheological property of the geobelt could also contribute to the differences of pullout forces in post-peak stage. The specimens in pullout tests were loaded with a constant rate of 1 mm/min. The rheological property of the geobelt would increasingly influence the pullout process. In general, reasonably good agreement between numerical and tested results during the whole pull-out test range including ones after the pull-out test peak load could demonstrate the validity of the pullout behavior model involving the strain-softening model of geobelt–clay interaction and the hyperbolic model of full stress–strain curve of the geobelt.

Strain distribution of geobelt in pullout process

By investigating different moments in the pullout process, the evolution of the strain distribution alongside the geobelt could be reflected. Given that the strain of the geobelt is closely related to the tensile force, several front pullout forces in the pullout process are selected. Taking advantage of the tensoresistivity of SEGB, the strain of the geobelt could be calculated according to eq. 1 by measuring the changes of electrical resistance in pullout tests, which therefore could be utilized as a convenient method to validate the numerical results of the strain distribution. Taking the case of the compaction degree of 96% as an example, Fig. 14 shows the tested and numerical strain distributions with different normal pressures and front pullout force levels (50%, 75%, and 100% of $F_{0\,m}$), where $F_{0\,m}$ is defined as the maximum value of front pullout force.

Fig. 13. Front pullout force–displacement curves in pullout tests: (*a*) compaction degree: 90%; (*b*) compaction degree: 96%. [Color online.]

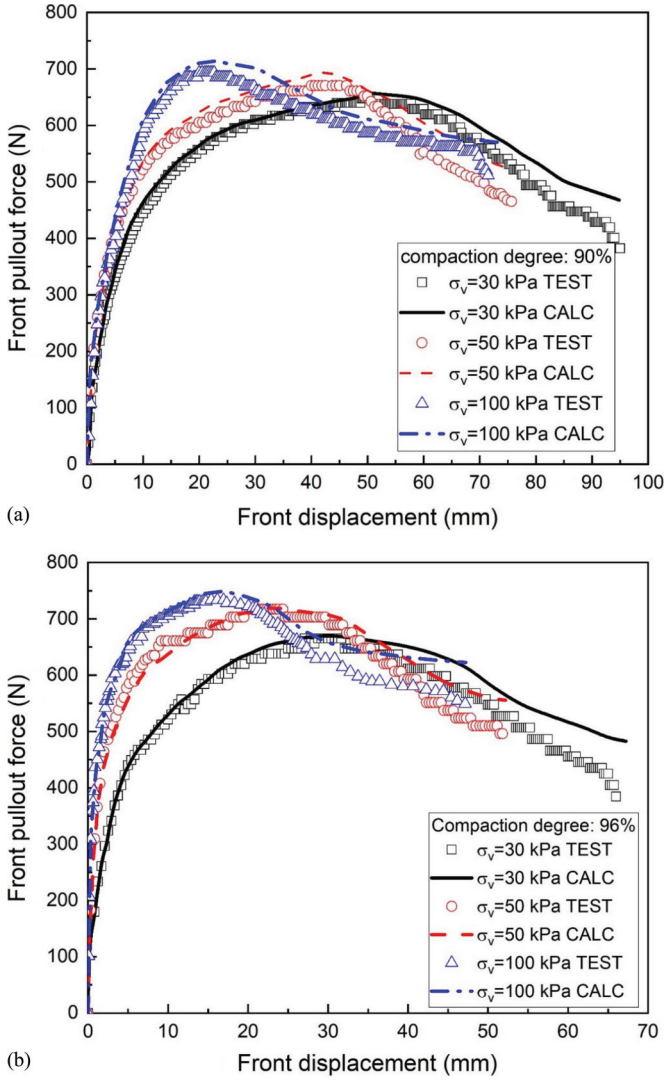

Fig. 14. Strain distribution of SEGB: (*a*) σ_v = 30 kPa; (*b*) σ_v = 50 kPa; (*c*) σ_v = 100 kPa. [Color online.]

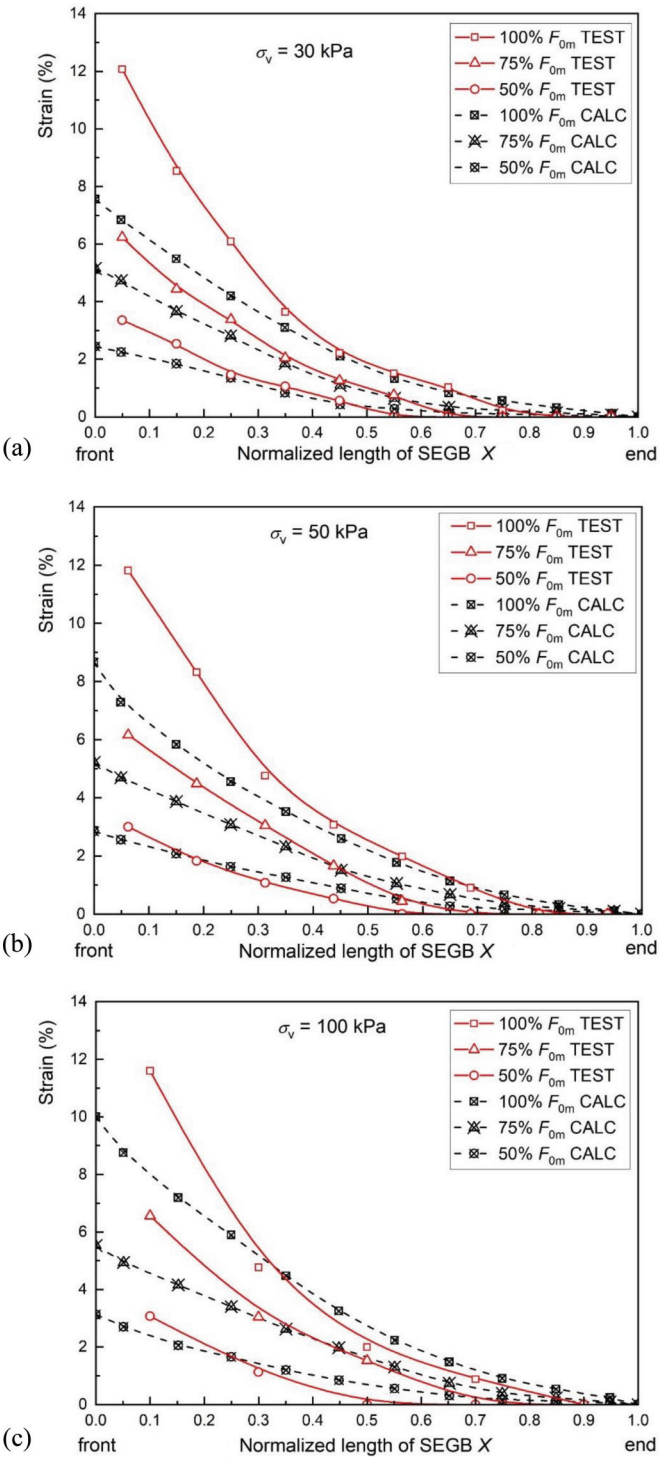

For three scenarios of normal pressures applied, the numerical and tested results share the same trend that the deformation of the geobelt started from the front end, and then progressively delivered towards the tail end. However, the tested results were generally higher than the numerical results at the front end, especially in the cases of 100% and 75% $F_{0\ m}$. There may be two reasons for the underestimation of the front-end strain in numerical results. One is the underestimation on strain in the hyperbolic model, especially in high level of tensile stress, as mentioned previously. The other one could be attributed to the boundary condition from testing apparatus. Although the clamping system in the horizontal pulling system could guarantee no rupture of the specimens in the clamp, the front end of the specimen was exposed to the air when the specimen was pulled out from the test chamber due to the absence of a metal sleeve from the testing apparatus. The unconfined surroundings could result in larger measured strains at the front end of the specimen, and the specimen was prone to rupture in the gap between the test chamber and the clamp.

It also can be found that there is a slight difference between tested and the numerical results for parts of the geobelt closing to the tail end. This may be induced by the sensitivity of the measurements that can refer to two aspects. One is related to the tensoresistivity of SEGB itself. As the tensoresistivity of SEGB is derived from the piezoresistive effect, it is possible that the deformation is so subtle that the electrical resistance is unchanged. This influence involves many factors such as the length of measuring zones and temperature. The other one is the insufficient sensitivity of measuring instruments.

Fig. 15. Numerical results (F_0 = 100% $F_{0\ m}$) with different normal pressures and compaction degrees: (*a*) displacement distribution; (*b*) shear stress distribution. [Color online.]

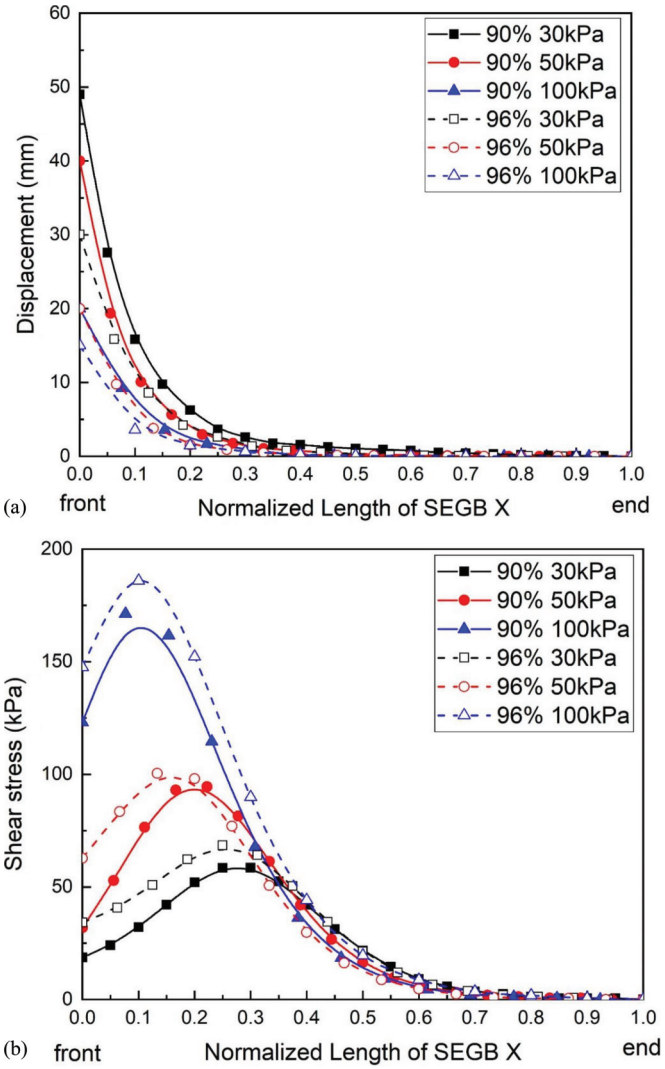

Comparisons and analysis of numerical results of interfacial behavior

The calculated distributions of displacement and shear stress along SEGB are compared for different cases (normal pressures and compaction degrees) at 100% of $F_{0\ m}$ in Figs. 15*a* and 15*b*, respectively.

The numerical results in Fig. 15*a* show that the displacement of the geobelt decreased sharply in the area close to the front end (the first 20% section of the SEGB), then decreased slowly in the rest area. Also, the displacements at the front end of the geobelts for the lower compaction degree were generally larger than the counterpart at the same normal pressure and the same trend can be found for the smaller normal pressure at the same compaction degree.

With the strain-softening response at the interfaces, the interfacial shear stress shows different distributions in Fig. 15*b*. The interfacial shear stress obviously increased with the increasing normal pressure, but slightly increased with the increasing compaction degree. This verifies that the normal pressure has larger influence on the geobelt–clay interaction than the compaction degree. Additionally, the normal pressure also has great effect on the position of the maximum shear stress. With the higher normal pressure applied in pullout test, the location corresponding to the maximum value of interfacial shear stress was closer to the front end.

Discussion

The geosynthetic–soil interface interaction has been studied with the assumption of many theoretical models, such as bilinear model (Madhav et al. 1998), hyperbolic model (Gurung 2001), and rigid – perfectly plastic model (Zornberg et al. 2017). All these models were established based on direct shear tests, and then were directly incorporated in the pullout test analyses. Similarly, it is assumed in this study that the geobelt axial displacement (u in eq. 17) is the same as the interface relative shear displacement (u in eq. 1). Based on this assumption, the strain-softening model could be incorporated in the deduction of load transfer equation. However, during the process of pulling out geobelts from the confining soil, shear stress $\tau(x)$ along the geobelt–soil interface was mobilized by the pullout force on the geobelt, which might lead to movements of the soil particles near the interfaces. Further attempts are still needed to take the movement of soil particles at interfaces into consideration in both theoretical analysis and test measurement.

According to ASTM (2013) standard D6706-01, a metal sleeve at the aperture located in the front face of the pullout box is designed to transfer the force into the soil and reduce the stress on the aperture of the pullout box. Once the stress was concentrated on the aperture of the pullout box, the soil particles would run out through the aperture on the door, causing the loss of soil. It seems that the absence of metal sleeves resulted in unconfined specimen, particularly at the front part of geosynthetics and may accordingly cause a larger measurement of the strains at those locations. Attempts made to minimize the impact of the clamp system without a sleeve included (*i*) the unconfined length of geobelts controlled within 10 mm before the commencement of pullout tests through moving the clamp as close as possible to the front face of the pullout box and (*ii*) no slippage guaranteed between the clamp and the geobelts through employing rubber sheets and high strength bolts–screws. Further studies on this issue may be worthwhile, as neither Wang et al. (2016) nor Wang et al. (2019) incorporated the metal sleeve into the testing apparatus.

Conclusions

A theoretical model for evaluating the pullout behavior of geobelts was proposed by incorporating the strain-softening model verified by direct shear tests and a hyperbolic model capturing the stress–strain curves of geobelts. The proposed model was numerically solved and validated by a series of pullout tests. The pullout tests were performed with the same compaction degrees (90% and 96%) as tested in direct shear tests. A kind of sensor-enabled geobelt (SEGB) was employed in all the tests mentioned above. The tensoresistivity performance of SEGBs, which enabled strains to be measured based on piezoresistive effect, was also utilized as a new method for deformations measurement in pullout tests to compare with the numerical results. The comparisons between the numerical results and tested results lead to the following conclusions:

1. The numerical results reasonably matched measured data in pullout tests in terms of front pullout force–displacement curves and strain distributions. Although the proposed model slightly overestimated the pullout forces in the post-peak stage, the theoretical model gave an effective description of the strain-softening behavior of the geobelts during the pullout tests. Also, the strain-softening model of geobelt–clay interfaces based on direct shear test results was effective.
2. The increase of compaction degree in pullout tests resulted in smaller front displacement, mobilizing the peak value of the front pullout force, yet having less effect on the interfacial shear stress than the normal pressure. Higher normal pres-

sure led to the occurrence of the maximum shear stress at a closer position to the front end of SEGB.

3. SEGB proved to be an effective method for the strain measurements of in-soil geosynthetics. On one hand, the strain distributions measured by SEGBs validated the effectiveness of the proposed pullout behavior analysis model, including the strain-softening model and the hyperbolic model. On the other hand, SEGBs demonstrated the working process during the pullout tests. With the measured results from SEGBs, it became evident that the deformation of the geobelt in pullout tests started from the front end and progressively delivered towards the tail end.

Acknowledgements

The authors are grateful to the support of the National Key Research and Development Project (2018YFB1600100), Natural Science Foundations of China (51778346; 51608461), and Shandong Key Research and Development Project (2017GGX50102).

References

Abd, A.H., and Utili, S. 2017. Design of geosynthetic-reinforced slopes in cohesive backfills. Geotextiles and Geomembranes, **45**(6): 627–641. doi:10.1016/j.geotexmem.2017.08.004.

Abdelouhab, A., Dias, D., and Freitag, N. 2010. Physical and analytical modelling of geosynthetic strip pull-out behavior. Geotextiles and Geomembranes, **28**(1): 44–53. doi:10.1016/j.geotexmem.2009.09.018.

Anubhav, S., and Basudhar, P.K. 2010. Modeling of soil-woven geotextile interface behavior from direct shear test result. Geotextiles and Geomembranes, **28**(4): 403–408. doi:10.1016/j.geotexmem.2009.12.005.

ASTM. 2007. Standard test methods for geosynthetics. ASTM standard D6637-01. American Society for Testing and Materials, West Conshohocken, Pa, USA.

ASTM. 2011. Standard practice for classification of soils for engineering purposes (Unified Soil Classification System). ASTM standard D2487. American Society for Testing and Materials, West Conshohocken, Pa, USA.

ASTM. 2013. Standard test method for measuring geosynthetic pullout resistance in soil. ASTM standard D6706-01. American Society for Testing and Materials, West Conshohocken, Pa, USA.

ASTM. ASTM standard 2017. Standard test method for determining the shear strength of soil-geosynthetic and geosynthetic-geosynthetic interfaces by direct shear. ASTM standard D5321. American Society for Testing and Materials, West Conshohocken, Pa, USA.

Bathurst, R.J., and Ezzein, F.M. 2017. Insights into geogrid-soil interaction using a transparent granular soil. Géotechnique Letter, **7**(2s): 179–183. doi:10.1680/jgele.16.00191.

Chai, J.-C., and Saito, A. 2016. Interface shear strengths between geosynthetics and clayey soils. International Journal of Geosynthetics and Ground Engineering, **2**: 19. doi:10.1007/s40891-016-0060-8.

Chawla, S., and Shahu, J.T. 2016. Reinforcement and mud-pumping benefits of geosynthetics in railway tracks: model tests. Geotextiles and Geomembranes, **44**(3): 366–380. doi:10.1016/j.geotexmem.2016.01.005.

Chen, Q., and Abu-Farsakh, M. 2016. Mitigating the bridge end bump problem: a case study of a new approach slab system with geosynthetic reinforced soil foundation. Geotextiles and Geomembranes, **44**(1): 39–50. doi:10.1016/j.geotexmem.2015.07.001.

Choudhary, A.K., and Krishna, A.M. 2016. Experimental investigation of interface behaviour of different types of granular soil/geosynthetics. International Journal of Geosynthetics and Ground Engineering, **2**: 4. doi:10.1007/s40891-016-0044-8.

Cui, X.Z., Cui, S.Q., Jin, Q., Wang, Y.L., Zhang, L., and Wang, Z.X. 2018*a*. Laboratory tests on the engineering properties of sensor-enabled geobelts (SEGB). Geotextiles and Geomembranes, **46**(1): 66–76. doi:10.1016/j.geotexmem.2017.10.004.

Cui, X.Z., Cui, S.Q., Wang, Y.L., and Li, J. 2018*b*. Laboratory tests on the engineering properties of sensor-enabled geobelts (SEGB) - a reply to the discussion. Geotextiles and Geomembranes, **46**(5): 681–683. doi:10.1016/j.geotexmem.2018.06.002.

Cui, X.Z., Wang, Y.L., Liu, K.W., Wang, X.Z., Jin, Q., Zhao, M.L., and Cui, S.Q. 2019. A simplified model for evaluating the hardening behavior of sensor-enabled geobelts during pullout tests. Geotextiles and Geomembranes, **47**(3): 377–388. doi:10.1016/j.geotexmem.2019.01.007.

Esterhuizen, J.J.B., Fliz, G.M., and Duncan, J.M. 2001. Constitutive behavior of geosynthetic interface. Journal of Geotechnical and Geoenvironmental Engineering, **127**(10). doi:10.1061/(ASCE)1090-0241(2001)127:10(834).

Ezzein, F.M., Bathurst, R.J., and Kongkitkul, W. 2015. Nonlinear load-strain modeling of polypropylene geogrids during constant rate-of-strain loading. Polymer Engineering & Science, **55**(7): 1617–1627. doi:10.1002/pen.23999.

Gurung, N. 2001. 1-D analytical solution for extensible and inextensible soil/rock reinforcement in pull-out tests. Geotextiles and Geomembranes, **19**(4): 195–212. doi:10.1016/S0266-1144(01)00008-5.

Gurung, N., and Iwao, Y. 1999. Numerical simulation of pullout response for planar soil reinforcements. Canadian Geotechnical Journal, **36**(3): 455–466. doi:10.1139/t99-006.

Hatami, K., Grady, B., and Ulmer, M. 2009. Sensor-enabled geosynthetics: use of conducting carbon networks as geosynthetic sensors. Journal of Geotechnical and Geoenvironmental Engineering, **135**(7). doi:10.1061/(ASCE)GT.1943-5606.0000062.

Infante, D.J.U., Martinez, G.M.A., Arrua, P.A., and Eberhardt, M. 2016. Shear strength behavior of different geosynthetic reinforced soil structure from direct shear test. International Journal of Geosynthetics and Ground Engineering, **2**: 17. doi:10.1007/s40891-016-0058-2.

Li, J., Cui, X.Z., Jin, Q., Su, J.W., Cui, S.Q., and Wang, Y.L. 2018. Laboratory investigation of the durability of a new smart geosynthetic material. Construction and Building Materials, **169**: 28–33. doi:10.1016/j.conbuildmat.2018.02.187.

Liu, H.B. 2016. Nonlinear elastic analysis of reinforcement loads for vertical reinforced soil composites without facing restriction. Journal of Geotechnical and Geoenvironmental Engineering, **142**(6). doi:10.1061/(ASCE)GT.1943-5606.0001464.

Liu, H.B., Yang, G.Q., and Hung, C. 2017*a*. Analyzing reinforcement loads of vertical geosynthetic-reinforced soil walls considering toe restraint. International Journal of Geomechanics, **17**(6). doi:10.1061/(ASCE)GM.1943-5622.0000840.

Liu, H.B., Yang, G.Q., Wang, H., and Xiong, B.L. 2017*b*. A large-scale test of reinforced soil railway embankment with soilbag facing under dynamic loading. Geomechanics and Engineering, **12**(4): 579–593. doi:10.12989/gae.2017.12.4.579.

Liu, K.W., Rowe, R.K., Su, Q., Liu, B., and Yang, Z.X. 2017. Long-term reinforcement strains for column supported embankments with viscous reinforcement by FEM. Geotextiles and Geomembranes, **45**: 307–319. doi:10.1016/j.geotexmem.2017.04.003.

Liu, K.W., Su, Q., Ni, P.P., Zhou, C.B., and Yue, F. 2018. Evaluation on the dynamic performance of bridge approach backfilled with fibre reinforced lightweight concrete under high-speed train loading. Computers and Geotechnics, **104**: 42–53. doi:10.1016/j.compgeo.2018.08.003.

Madhav, M.R., Gurung, N., and Iwao, Y. 1998. A theoretical model for the pull-out response of geosynthetic reinforcement. Geosynthetics International, **5**(4): 399–424. doi:10.1680/gein.5.0128.

Mitchell, J.K., and Zornberg, J. 1995. Reinforced soil structures with poorly draining backfills. Part II: case histories and applications. Geosynthetics International, **2**(1): 265–307. doi:10.1680/gein.2.0011.

Mosallanezhad, M., Taghavi, S.H.S., Hataf, N., and Alfaro, M.C. 2016. Experimental and numerical studies of the performance of the new reinforcement system under pull-out conditions. Geotextiles and Geomembranes, **44**(1): 70–80. doi:10.1016/j.geotexmem.2015.07.006.

Mousavi, S.E. 2017. Shear strength behavior in the interface of contaminated soil with bio-diesel oil and geosynthetics. Transportation Geotechnics, **10**: 62–72. doi:10.1016/j.trgeo.2016.12.003.

Portelinha, F.H.M., Bueno, B.S., and Zornberg, J.G. 2013. Performance of nonwoven geotextile-reinforced walls under wetting conditions: laboratory and field investigations. Geosynthetics International, **20**(2): 90–104. doi:10.1680/gein.13.00004.

Punetha, P., Mohanty, P., and Samanta, M. 2017. Microstructural investigation on mechanical behavior of soil-geosynthetic interface in direct shear test. Geotextiles and Geomembranes, **45**(3): 197–210. doi:10.1016/j.geotexmem.2017.02.001.

Racana, N., Grédiac, M., and Gourvès, R. 2003. Pull-out response of corrugated geotextile strips. Geotextiles and Geomembranes, **21**(5): 265–288. doi:10.1016/S0266-1144(03)00031-1.

Rousé, P.C., Fannin, R.J., and Taiebat, M. 2014. Sand strength for back-analysis of pull-out tests at large displacement. Géotechnique, **64**(4): 320–324. doi:10.1680/geot.13.T.021.

Rowe, R.K., and Liu, K.W. 2015. Three-dimensional finite element modelling of a full-scale geosynthetic-reinforced, pile-supported embankment. Canadian Geotechnical Journal, **52**(12): 2041–2054. doi:10.1139/cgj-2014-0506.

Sadat Taghavi, H.S., and Mosallanezhad, M. 2017. Experimental analysis of large-scale pullout tests conducted on polyester anchored geogrid reinforcement systems. Canadian Geotechnical Journal, **54**(5): 621–630. doi:10.1139/cgj-2016-0365.

Seo, M.W., Park, I.J., and Park, J.B. 2004. Development of displacement-softening model for interface shear behavior between geosynthetics. Soils and Foundations, **44**(6): 27–38. doi:10.3208/sandf.44.6_27.

Shahin, H.M., Nakai, T., Morikawa, Y., Masuda, S., and Mio, S. 2017. Effective use of geosynthetics to increase bearing capacity of shallow foundations. Canadian Geotechnical Journal, **54**(12): 1647–1658. doi:10.1139/cgj-2016-0505.

Shen, P., Xu, C., and Han, J. 2018. Model tests investigating spatial tensile behavior of simulated geosynthetic reinforcement material over rigid supports. Journal of Materials and Civil Engineering, **30**(2). doi:10.1061/(ASCE)MT.1943-5533.0002156.

Tano, B.F.G., Stoltz, G., Touze-Foltz, N., Dias, D., and Olivier, F. 2017. A numerical modelling technique for geosynthetics validated on a cavity model test. Geotextiles and Geomembranes, **45**(4): 339–349. doi:10.1016/j.geotexmem.2017.04.006.

Wang, H.L., Chen, R.P., Liu, Q.W., Kang, X., and Wang, Y.W. 2019. Soil–geogrid interaction at various influencing factors by pullout tests with applications of FBG sensors. Journal of Materials in Civil Engineering, **31**(1). doi:10.1061/(ASCE)MT.1943-5533.0002537.

Wang, J.Q., Zhou, Y.F., Tang, X.Y., and Huang, S.B. 2017. Development and application of large size direct shear test apparatus with visual and digital collection functions for reinforced soil. Rock and Soil Mechanics, **38**(5): 1533–1540. doi:10.16285/j.rsm.2017.05.038.

Wang, Z., Jacobs, F., and Ziegler, M. 2016. Experimental and DEM investigation of geogrid–soil interaction under pullout loads. Geotextiles and Geomembranes, **44**(3): 230–246. doi:10.1016/j.geotexmem.2015.11.001.

Xiao, M., Ledezma, M., and Hartman, C. 2015. Shear resistance of tire-derived aggregate using large-scale direct shear tests. Journal of Materials in Civil Engineering, **27**(1). doi:10.1061/(ASCE)MT.1943-5533.0001007.

Xie, Y., and Leshchinsky, B. 2015. MSE walls as bridge abutments: Optimal reinforcement density. Geotextiles and Geomembranes, **43**(2): 128–138. doi:10.1016/j.geotexmem.2015.01.002.

Yu, Y., and Bathurst, R.J. 2017*a*. Influence of selection of soil and interface properties on numerical results of two soil–geosynthetic interaction problems. International Journal of Geomechanics, **17**(6). doi:10.1061/(ASCE)GM.1943-5622.0000847.

Yu, Y., and Bathurst, R.J. 2017*b*. Modelling of geosynthetic-reinforced column-supported embankments using 2D full-width model and modified unit cell approach. Geotextiles and Geomembranes, **45**(2): 103–120. doi:10.1016/j.geotexmem.2017.01.002.

Yu, Y., and Bathurst, R.J. 2017*c*. Probabilistic assessment of reinforced soil wall performance using response surface method. Geosynthetics International, **24**(5): 524–542. doi:10.1680/jgein.17.00019.

Yu, Y., Bathurst, R.J., and Damians, I.P. 2016*a*. Modified unit cell approach for modelling geosynthetic-reinforced column-supported embankments. Geotextiles and Geomembranes, **44**(3): 332–343. doi:10.1016/j.geotexmem.2016.01.003.

Yu, Y., Bathurst, R.J., Allen, T.M., and Nelson, R. 2016*b*. Physical and numerical modelling of a geogrid-reinforced incremental concrete panel retaining wall. Canadian Geotechnical Journal, **53**(12): 1883–1901. doi:10.1139/cgj-2016-0207.

Zhang, F., Gao, Y., Leshchinsky, D., Yang, S., and Dai, G. 2018. 3D effects of turning corner on stability of geosynthetic-reinforced soil structures. Geotextiles and Geomembranes, **46**(4): 367–376. doi:10.1016/j.geotexmem.2018.03.001.

Zhang, Q.Q., and Zhang, Z.M. 2012. A simplified nonlinear approach for single pile settlement analysis. Canadian Geotechnical Journal, **49**(11): 1256–1266. doi:10.1139/t11-110.

Zornberg, J., and Mitchell, J.K. 1994. Reinforced soil structures with poorly draining backfills. Part I: reinforcement interactions and functions. Geosynthetics International, **1**(2): 103–148. doi:10.1680/gein.1.0006.

Zornberg, J.G., Roodi, G.H., and Gupta, R. 2017. Stiffness of soil–geosynthetic composite under small displacements: i. model development. Journal of Geotechnical and Geoenvironmental Engineering, **143**(10). doi:10.1061/(ASCE)GT.1943-5606.0001768.

List of symbols

A	cross-sectional area of geobelt
a	coefficient in hyperbolic model ($= \eta(\dot{\varepsilon})$)
b	coefficient in hyperbolic model ($= 1/J_0(\dot{\varepsilon})$)
C_c	coefficient of curvature of clay
C_u	uniformity coefficient of clay
c_{sg}	peak apparent cohesion of interfacial friction
E_s	initial shear modulus of geobelt–clay interface
F	tensile force
$F_{0\,m}$	maximum value of front pullout force
h	length of each discretized element
i	node number of discretized elements
I_P	plasticity index of clay
J_0	strain-rate-dependent initial axial stiffness of geobelt
l	length of geobelt
n	number of discretized elements of geobelt
p	parameter of strain softening model
q	parameter of strain softening model
R_0	initial value of electrical resistance
R_s	measured value of electrical resistance after deformation
r	parameter of strain softening model
T	tensile stress of geobelt
U	nondimensionalized displacement
u	interface relative shear displacement
u_m	relative displacement regarding maximum value of interfacial shear stress
u_∞	infinity of relative displacement
$u(0)$	front displacement from pullout results
w	width of geobelt
w_L	liquid limit of clay
X	nondimensionalized position of geobelt
x	position along geobelt
α	tensoresistivity coefficient
β	tensoresistivity coefficient
β_r	ratio of residual shear stress to maximum shear stress at geobelt–clay interfaces
ε	strain of geobelt
$\dot{\varepsilon}$	strain rate of geobelt
η	strain-rate-dependent scaling factor in geobelt model
τ	interfacial shear stress
τ_m	maximum value of geobelt–clay interfacial shear stress
τ_r	residue shear stress
σ_v	vertical–normal pressure
φ_r	residual angle of interfacial friction
φ_{sg}	peak angle of interfacial friction